NANO LETTERS

pubs.acs.org/NanoLett Letter

In Situ Imaging of Catalytic Reactions on Tungsten Oxide Nanowires Connects Surface–Ligand Redox Chemistry with Photocatalytic Activity

Meikun Shen, Tianben Ding, Che Tan, William H. Rackers, Dongyan Zhang, Matthew D. Lew, and Bryce Sadtler*

Cite This: *Nano Lett.* 2022, 22, 4694–4701 Read Online

ACCESS | Metrics & More | Article Recommendations | Supporting Information

ABSTRACT: Semiconductor nanocrystals are promising candidates for generating chemical feedstocks through photocatalysis. Understanding the role of ligands used to prepare colloidal nanocrystals in catalysis is challenging due to the complexity and heterogeneity of nanocrystal surfaces. We use *in situ* single-molecule fluorescence imaging to map the spatial distribution of active regions along individual tungsten oxide nanowires before and after functionalizing them with ascorbic acid. Rather than blocking active sites, we observed a significant enhancement in activity for photocatalytic water oxidation after treatment with ascorbic acid. While the initial nanowires contain inactive regions dispersed along their length, the functionalized nanowires show high uniformity in their photocatalytic activity. Spatial colocalization of the active regions with their surface chemical properties shows that oxidation of ascorbic acid during photocatalysis generates new oxygen vacancies along the nanowire surface. We demonstrate that controlling surface–ligand redox chemistry during photocatalysis can enhance the active site concentration on nanocrystal catalysts.

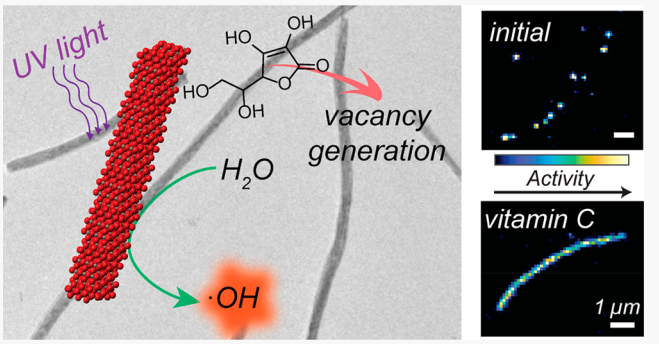

KEYWORDS: *single-molecule localization microscopy, surface functionalization, nanowires, oxygen vacancies, photocatalysis*

Colloidal semiconductor nanocrystals are actively being studied as photocatalysts for fuel production and environmental remediation.[1−20] The small dimensions of nanocrystals efficiently suppress the bulk recombination of photoexcited charge carriers due to the short diffusion distances required to reach the surface.[10,21−23] However, the fate of photoexcited charges once they reach the surface, that is, whether they recombine or are extracted to initiate useful redox reactions, is highly sensitive to the structure of the surface. Organic ligands that bind to atoms on the nanocrystal surface are commonly used to control the size and shape of colloidal metal and semiconductor nanocrystals.[4,24−27] Residual ligands that block access to the particle surface can poison the nanocatalyst.[1−4,28] However, recent studies have shown that organic ligands can tune the activity and selectivity of nanocatalysts by regulating competitive adsorption of substrate molecules and inhibitors to surface sites, changing the electronic structure at the surface, and/or acting as redox shuttles to facilitate interfacial charge transfer.[4−6,28−42] Although controlling surface–ligand interactions is critical in the design of nanocatalysts, conventional measurements of catalytic activity only provide ensemble-averaged structure–activity trends. The complexity of nanocrystal surfaces makes it challenging to determine the local environment of active sites and the role of ligands in controlling catalytic activity.

Single-molecule localization microscopy can overcome the limitations of ensemble-averaging to identify both inter- and intraparticle heterogeneity in the reactivity of nanostructured catalysts.[43−66] This super-resolution optical technique uses fluorogenic probes that are chemically activated into their fluorescence state to monitor catalytic turnover events *in situ* at the single-molecule and single-particle scales. However, a limitation of single-molecule imaging is that the fluorogenic probes used to visualize reaction events do not directly report on the chemical properties that lead to nanoscale variations in activity. To overcome this limitation, we have used the spatial colocalization of two complementary fluorogenic probes to elucidate the nature of active sites in semiconductor photocatalysts.[61,62] We previously applied this technique to tungsten

Received: February 17, 2022
Revised: June 2, 2022
Published: June 8, 2022

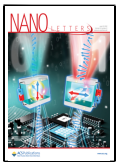

https://doi.org/10.1021/acs.nanolett.2c00674
Nano Lett. 2022, 22, 4694–4701

oxide, $W_{18}O_{49}$, nanowires which is a promising photocatalyst for water oxidation,[10,14−20] to show that the nanowires possess nanoscale segments of active regions separated by inactive regions along their lengths.[62] Through the colocalization of two independent fluorogenic probes, one activated by hydroxyl radicals (•OH) and the other activated by surface Lewis acidic sites (i.e., tungsten ions exposed by oxygen vacancies), we revealed that clusters of oxygen vacancies are distributed nonuniformly along the $W_{18}O_{49}$ nanowires and serve as active sites for the photocatalytic generation of •OH radicals. Thus, it is the regions containing low concentrations of oxygen vacancies in each nanowire that limit the photocatalytic activity of this material.

Here, we use *in situ* single-molecule imaging to elucidate the activity change mediated by surface functionalization of a metal oxide photocatalyst. We compare the spatial distribution of active regions in $W_{18}O_{49}$ nanowires before and after functionalizing them with ascorbic acid, which is a common ligand used in nanoparticle synthesis.[27,67,68] Rather than block the surface of the nanowires, we find that ascorbic acid is oxidized *in situ* during photocatalysis to generate new active sites (i.e., oxygen vacancies). Unlike the as-synthesized $W_{18}O_{49}$ nanowires, single-molecule imaging shows a highly uniform distribution of active regions in the functionalized nanowires, which enhances their photocatalytic activity at both the ensemble level (oxygen evolution rates of 100 μmol/h for the functionalized nanowires versus 54 μmol/h for the as-synthesized ones) and single-molecule level (per nanowire rate constants of 442 $\mu m^{-1}\cdot min^{-1}$ for the functionalized nanowires vs 248 $\mu m^{-1}\cdot min^{-1}$ for the as-synthesized ones).

Tungsten oxide nanowires were synthesized via a hydrothermal method as described previously.[62] The nanowires possess the monoclinic $W_{18}O_{49}$ phase as evidenced by X-ray diffraction (Figure S1). They have an average diameter of 11 ± 3 nm (average ± first standard deviation), lengths of several microns, and grow along the [010] direction (Figure 1a and Figure S2). X-ray photoelectron spectra (XPS) show that tungsten ions in the nanowires possess a mixture of the +6, + 5, and +4 oxidation states (Figure 1c).[14,19,20,69] The lower oxidation states of tungsten are charge compensated by oxygen vacancies. XPS in the region for O 1s electrons show a peak corresponding to oxygen within the tungsten oxide nanowires along with a shoulder peak at higher binding energy (Figure S3). This shoulder peak is typically attributed to oxygen-containing species that bind to metal ions exposed by surface oxygen vacancies.[17,19,69] Further evidence of oxygen vacancies comes from the absorption spectrum of the nanowires (Figure S4). Absorption at wavelengths below 450 nm corresponds to band gap absorption, while a broad feature starting at 600 nm and going into the near-infrared results from free-carrier absorption due to the mixture of oxidation states for tungsten and surface oxygen vacancies.[14,15,17,19,20] Oxidation of the $W_{18}O_{49}$ nanowires to fill the oxygen vacancies removes the free-carrier absorption (Figure S4) and leads to tungsten ions in predominantly the +6 oxidation state as evidenced by XPS.[14,62]

We next functionalized the as-synthesized $W_{18}O_{49}$ nanowires with ascorbic acid (see Section 4 of the Supporting Information for details). Infrared (IR) spectra of the functionalized nanowires show characteristic peaks corresponding to ascorbic acid between 1000 and 1800 cm^{-1} as well as metal−oxygen stretches between 500 and 1000 cm^{-1} (see Figure 1b and Figure S5). XPS did not show a significant

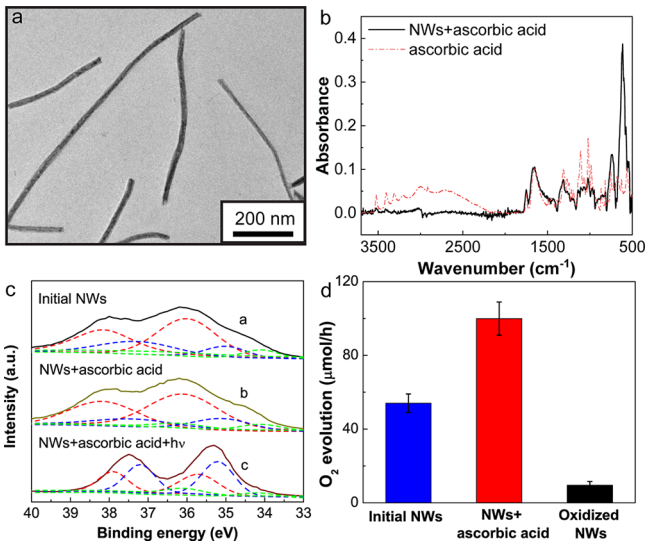

Figure 1. (a) Transmission electron microscopy image of the as-synthesized $W_{18}O_{49}$ nanowires. (b) Infrared absorbance spectrum of neat ascorbic acid (dotted, red trace) and a difference spectrum of the infrared absorbance of ascorbic acid-functionalized $W_{18}O_{49}$ nanowires and the as-synthesized nanowires (solid, black trace). (c) XPS in the binding energy region for W 4f electrons of the as-synthesized $W_{18}O_{49}$ nanowires (a, black trace) and ascorbic acid-functionalized $W_{18}O_{49}$ nanowires before (b, dark-yellow trace) and after (c, red-brown trace) 5 min of laser irradiation. The dashed red, blue, and green lines for each spectrum show its deconvolution into contributions from W^{6+}, W^{5+}, and W^{4+}, respectively. (d) Ensemble production rates for photocatalytic oxygen evolution using the as-synthesized nanowires (blue, left bar), ascorbic acid-functionalized nanowires (red, middle bar), and oxidized nanowires (black, right bar).

change in the distribution of oxidation states for tungsten after functionalizing the nanowires with ascorbic acid (Figure 1c). Additional characterization of the surface charge and concentration of acid sites on the nanowires before and after functionalization (Table S2 and Sections 11 and 12) and discussion of the binding of ascorbic acid (Section 20) are provided in the Supporting Information.

Ensemble measurements showed that functionalization with ascorbic acid enhances the activity of the $W_{18}O_{49}$ nanowires for photocatalytic water oxidation. The as-synthesized nanowires exhibited an O_2 evolution rate of 54 μmol/h (Figure 1d). Because of binding of ascorbic acid to the surface of the nanowires, we initially expected a drop in photocatalytic activity after surface functionalization, as we previously observed for $W_{18}O_{49}$ nanowires coated with polyvinylpyrrolidone.[62] Surprisingly, the O_2 evolution rate for the ascorbic acid-functionalized $W_{18}O_{49}$ nanowires increased to 100 μmol/h (Figure 1d). Hydroxyl radical generation was quantified using fluorescence spectroscopy through the photocatalytic conversion of coumarin to 7-hydroxycoumarin (Figure S7).[70] The ascorbic acid-functionalized $W_{18}O_{49}$ nanowires also exhibited a higher production rate for •OH radicals, which is an intermediate in the photocatalytic oxidation of H_2O to O_2. On the other hand, oxidized nanowires in which oxygen vacancies were removed showed a significant drop in their production rate for O_2 (9 μmol/h, Figure 1d), consistent with prior work showing that oxygen vacancies increase the photocatalytic activity of metal oxide semiconductors.[14−16,19,20,62,71] Thus, we sought to understand how ascorbic acid-functionalization changes the concentration and

https://doi.org/10.1021/acs.nanolett.2c00674
Nano Lett. 2022, 22, 4694−4701

distribution of oxygen vacancies along the surface of the nanowires.

We used total internal reflection fluorescence (TIRF) microscopy to perform *in situ* imaging of catalytic reactions on the surface of the nanowires at the single-molecule level (see Supporting Information Sections 15 and 16 for details). We used 3′-(*p*-aminophenyl) fluorescein (APF) as a fluorogenic probe to detect the photocatalytic generation of •OH radicals (Figure 2a and Figure S9).[72] A solution containing APF and potassium iodate as a sacrificial oxidant was dropped onto a microscope coverslip with deposited nanowires. A 405 nm laser was used to excite the $W_{18}O_{49}$ nanowires, and a 488 nm laser was used to excite the fluorescent product (i.e., fluorescein). Only probe molecules activated at the catalyst surface produce sharp intensity bursts using TIRF imaging, while freely diffusing fluorescent molecules in solution lead to a weak fluorescent background. The turn-off of each fluorescence intensity burst is due to the desorption of the activated probe from the catalyst surface.[46−49,54−56,61−63] No fluorescence bursts were detected without the 405 nm laser. The localization precision of fluorescence bursts is 26 nm for APF (Figure S10). We fitted the point spread functions of all detected bursts over 2500 frames (i.e., 2.05 min using a 50 ms exposure time, see Supporting Information Sections 17 and 18 for details) (Figure 2b,d) and constructed activity maps for the photocatalytic •OH generation along individual nanowires (Figure 2c,e).

Representative activity maps of •OH generation for an as-synthesized nanowire and an ascorbic acid-functionalized nanowire are shown in Figure 2c,e. The activity maps plot the number of reaction events detected within 120 × 120 nm bins. Isolated active regions are observed for the as-synthesized nanowires as we previously reported[62] (see Figure 2c and Figure S14 for activity maps of the as-synthesized nanowires). Notably, the activity maps were completely altered after functionalization with ascorbic acid. Instead of isolated active regions, the functionalized nanowire shown in Figure 2e is active for •OH generation along its entire length. This change in activity was observed for all 20 nanowires imaged after functionalization (see Figure S15 additional activity maps of functionalized nanowires). The photon numbers and the on-times of fluorescence bursts do not change significantly after functionalization (see Figures S10−S13), indicating the activation of the nanowires is not an imaging artifact. Furthermore, adding a solution containing APF and ascorbic acid to a bare coverslip did not produce fluorescence bursts.

To further investigate the chemical properties of active regions along the nanowire surface, we sequentially imaged the same $W_{18}O_{49}$ nanowires using the two different probe molecules, APF for the photocatalytic generation of •OH and furfuryl alcohol (FA) to image the distribution of Lewis acid sites (Figure 3). By spatially correlating the activity for these two independent reactions,[62] we establish a link between the photocatalytically active regions along a nanowire and its spatial distribution of oxygen vacancies. While both Bronsted and Lewis acids can catalyze the condensation of FA to form highly fluorescent oligomers (Figure S16),[43,44,62] surface hydroxyl groups (i.e., Bronsted acid sites) of tungsten oxide are deprotonated when imaging activation of FA at pH 7.4 (supported by the negative zeta potential measured for the nanowires, see Table S2).[73] Therefore, we attribute the activation of this probe to tungsten ions exposed by oxygen vacancies, which act as Lewis acid sites. When imaging the

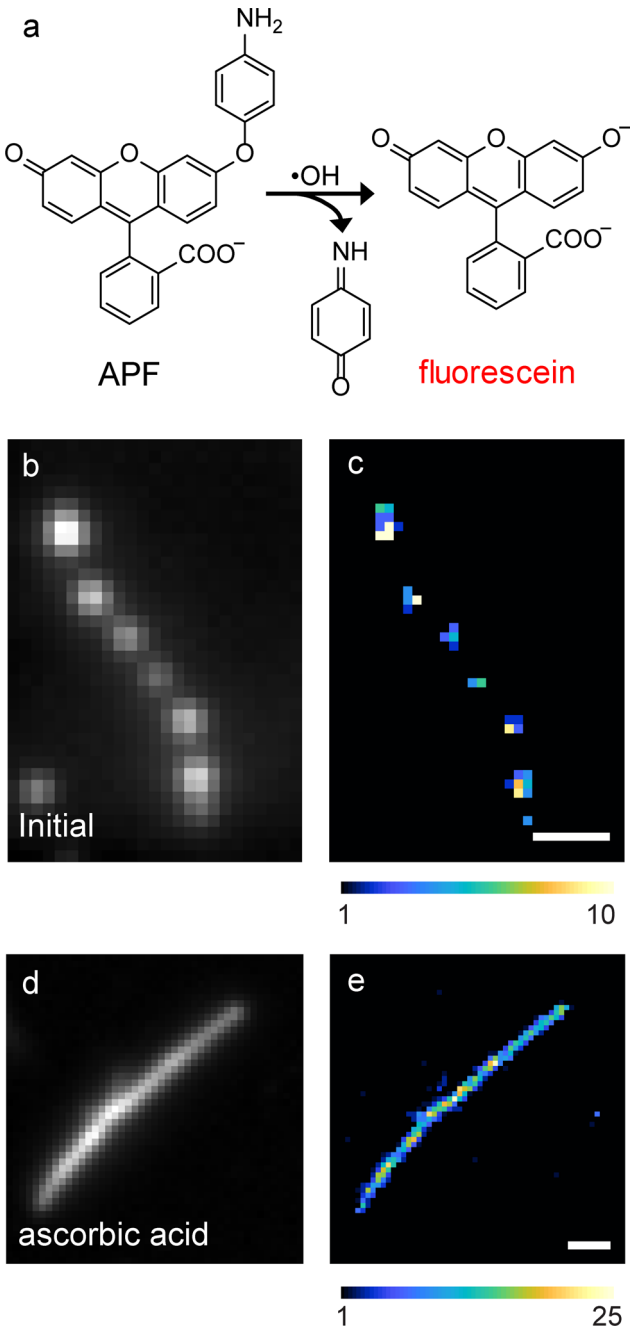

Figure 2. Single-molecule imaging of photocatalytic •OH generation on individual $W_{18}O_{49}$ nanowires. (a) Oxidation of APF by photocatalytically generated •OH radicals forms the highly fluorescent fluorescein. (b,d) Diffraction-limited fluorescence images of (b) a representative, as-synthesized nanowire and (d) an ascorbic acid-functionalized nanowire. (c,e) Super-resolution activity maps of the same (c) as-synthesized nanowire and (e) ascorbic acid-functionalized nanowire. Color scale: number of fluorescence bursts detected per bin (120 × 120 nm^2). Scale bars: 1 μm.

distribution of acid sites with FA, only a 561 nm laser (with a photon energy lower than the band gap of tungsten oxide) was used to excite the fluorescent oligomers. The localization precision of the fluorescence bursts is 24 nm for FA (Figure S11).

We used a coordinate-based colocalization (CBC) algorithm to quantify the degree of spatial colocalization between fluorescence bursts from each of the two probe mole-

https://doi.org/10.1021/acs.nanolett.2c00674
Nano Lett. 2022, 22, 4694−4701

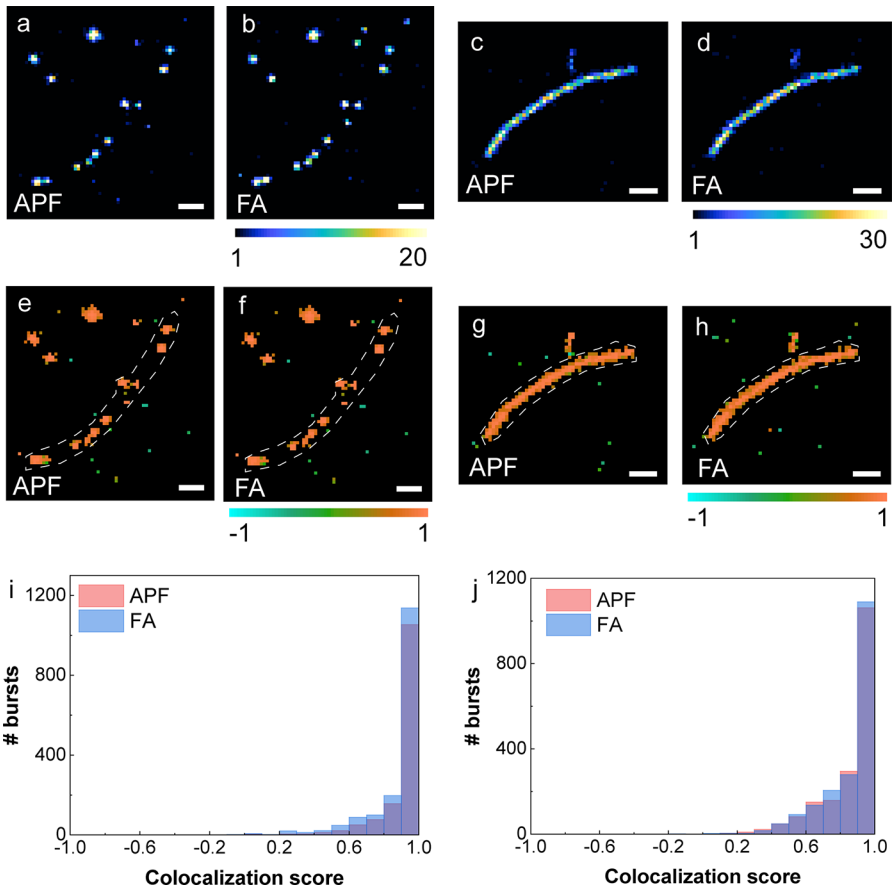

Figure 3. Spatial colocalization of photocatalytic •OH generation and Lewis acid sites for both a representative, as-synthesized $W_{18}O_{49}$ nanowire and an ascorbic acid-functionalized nanowire. Super-resolution activity maps of the two nanowires using (a,c) APF to detect •OH radicals and (b,d) furfuryl alcohol (FA) to identify Lewis acid sites via the condensation of FA. Color scale: number of fluorescence bursts detected per bin (120 × 120 nm^2). Coordinate-based colocalization (CBC) maps for fluorescence bursts using (e,g) APF and (f,h) FA. Color scale: median colocalization score in each bin ranging from −1 for anticorrelated to +1 for perfectly correlated. Scale bars: 1 μm. (i,j) Distribution of CBC scores for APF (red) and FA (blue) bursts showing a high degree of spatial correlation for the two reactions in both nanowires.

cules.[61,62,74] Each fluorescence burst in the two data sets is assigned a CBC score: +1 for a high degree of colocalization between the two probes and −1 if only one of the probes was detected in a specific region. (Details of the CBC algorithm and the procedure used to register the data sets obtained using the two fluorogenic probes are provided in Supporting Information Section 19.) Figure 3 shows representative CBC analysis on different $W_{18}O_{49}$ nanowires before and after ascorbic acid- functionalization. Orange regions in the colocalization maps in panels e, f, g, and h of Figure 3 represent areas of the nanowires that are active for both the photocatalytic generation of •OH and the acid-catalyzed condensation of FA. As we have previously reported for as-synthesized $W_{18}O_{49}$ nanowires,[62] the activity maps for both •OH generation and FA condensation show isolated active regions separated by inactive segments along the nanowire (Figure 3a,b). CBC analysis (Figure 3e,f,i) reveals that the same nanoscale regions are active for both reactions. As oxygen vacancies can catalyze these two independent transformations, their high degree of spatial correlation indicates that the distribution of oxygen vacancies is nonuniform along the nanowires and that regions with a high concentration of vacancies serve as the active sites for photocatalysis. We also observed a high degree of colocalization for the ascorbic acid-functionalized nanowires, as quantified by CBC analysis (Figure 3j). However, the functionalized nanowires no longer possessed inactive regions and displayed activity for both •OH generation (Figure 3c,g) and FA condensation (Figure 3d,h) along their entire length. The changes in super-resolution activity maps indicate that both the concentration of oxygen vacancies had increased, and their distribution had become more uniform along the functionalized nanowires (see Figures S14 and S15 for additional examples of colocalization analysis for both the as-synthesized and functionalized nanowires). Furthermore, while we observed a significant increase in the number of active regions, these regions possessed a similar distribution of specific activities (i.e., the number of fluorescence bursts detected per μm·min) compared to the initial nanowires (Figure S22). These results suggest that oxygen vacancies are introduced in regions that were initially inactive due to a low concentration of this defect.

We next characterized the compositional changes that occur in the ascorbic acid-functionalized nanowires during photocatalysis. Vibrational modes corresponding to ascorbic acid in the IR spectrum of the functionalized nanowires disappeared after irradiation (Figure S6). The functionalized nanowires exhibited an increase in absorption at near-infrared wavelengths after irradiation, consistent with an increase in the concentration of oxygen vacancies (Figure S4). For nanowires suspended in a solution of ascorbic acid and irradiated with a

https://doi.org/10.1021/acs.nanolett.2c00674
Nano Lett. 2022, 22, 4694−4701

xenon lamp, nuclear magnetic resonance (NMR) spectra showed a progressive decrease in the concentration of ascorbic acid with irradiation time (Figure S17). These observations indicate the removal of adsorbed ascorbic acid during photocatalysis. Films of functionalized $W_{18}O_{49}$ nanowires were also irradiated simultaneously with 405 and 488 nm lasers under the same conditions used for single-molecule imaging (see Section 8 of the Supporting Information for details). A decrease in the relative contribution of W^{6+} in the W 4f core level was observed only after irradiation (Figure 1c), indicating a reduction in the oxidation state of tungsten ions. Simultaneously, the shoulder peak in the O 1s spectrum increased after irradiation, consistent with the creation of new oxygen vacancies in the functionalized sample (Figure S3). In comparison, the as-synthesized nanowires do not undergo significant changes as evidenced by XPS when irradiated under the same conditions.[62] To confirm that photogenerated oxygen vacancies are indeed necessary to enhance the photocatalytic activity of the nanowires, we also performed single-molecule imaging of oxidized $W_{18}O_{49}$ nanowires with and without ascorbic acid. While no activity was detected on the bare oxidized nanowires (that contain a very low concentration of oxygen vacancies), we observed moderate activity for •OH generation after the oxidized nanowires were functionalized with ascorbic acid (see discussion below, Table S3, and Figures S18 and S19). These control experiments solidify the role of ascorbic acid in activating the nanowires by increasing the concentration of oxygen vacancies *in situ* during photocatalysis.

To quantify the enhancement in photocatalytic activity after ascorbic acid functionalization, we measured the concentration dependence of APF conversion at the single-molecule level (Figure 4). A series of different concentrations of APF (5−60 nM) was used to image the activity for •OH generation. The conversion rate of the surface-adsorbed probe into its activated form can be approximated as first order with its bulk concentration [APF] when the •OH concentration is much higher than [APF] and assuming that [•OH] remains constant during the reaction (due to the high concentrations of photoexcited carriers and H_2O).[47,49] This concentration dependence is often described by the Langmuir−Hinshelwood model in which the adsorption of APF is fast relative to its oxidation to fluorescein[46,47,49,54,56]

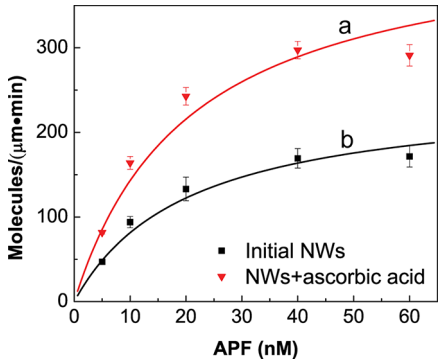

Figure 4. Concentration dependence of the specific activity for photocatalytic •OH generation at the single-molecule level for the initial nanowires (trace b, black squares) and ascorbic acid-functionalized nanowires (trace a, red triangles). The solid lines are fits to the Langmuir−Hinshelwood model (eq 1). Each data point represents the average of 20 nanowires, and the error bars show the standard deviation in specific activity for the 20 nanowires.

$$v = \frac{\gamma_{\text{eff}} K_{\text{ad}}[\text{APF}]}{1 + K_{\text{ad}}[\text{APF}]} \quad (1)$$

where v is the specific activity of detected product molecules for individual nanowires, K_{ad} is the equilibrium constant for adsorption of APF on the surface of a $W_{18}O_{49}$ nanowire, and γ_{eff} is the effective per-nanowire rate constant for •OH generation under the assumptions described above. For each concentration of APF, an average specific activity was determined by imaging 20 different nanowires. Figure 4 shows that for both the as-synthesized and ascorbic acid-functionalized $W_{18}O_{49}$ nanowires, v first increases and then saturates as [APF] increases, supporting the Langmuir−Hinshelwood model. We fitted the concentration dependence of v to eq 1. The rate constant for •OH generation, γ_{eff}, increased from 248 ± 19 $\mu m^{-1}\cdot min^{-1}$ (standard error) for the as-synthesized nanowires to 442 ± 42 $\mu m^{-1}\cdot min^{-1}$ for the ascorbic acid-functionalized nanowires. Oxidized nanowires were completely inactive, but they could be reactivated through functionalization to produce a γ_{eff} of 107 ± 13 $\mu m^{-1}\cdot min^{-1}$ (Figure S18). While the values of γ_{eff} were sensitive to these surface treatments, the values of K_{ad} were similar before (0.049 ± 0.008 nM^{-1}) and after functionalization (0.048 ± 0.012 nM^{-1}) (see Table S3 for the reaction constants after different surface treatments).

We next analyzed the on-times for fluorescence bursts, τ_{on}, which characterize the time each activated probe (i.e., fluorescein) remains adsorbed on the nanowire surface (Figure S20). As we did not observe a significant concentration dependence for τ_{on}, we assign the interparticle-averaged value of the inverse on-time, $\langle \tau_{\text{on}}^{-1} \rangle$, to the rate constant for self-dissociation of fluorescein from the nanowire, k_{d}.[46,47,54,63] Similar to K_{ad}, the value of k_{d} did not change significantly after functionalization (both at 0.048 ms^{-1}, Table S3). The consistency of K_{ad} and k_{d} for both samples indicates a similar chemical environment for the active regions of the nanowire surface. Therefore, we attribute the increase in γ_{eff} to more active sites generated along the functionalized nanowires during photocatalysis.

On the basis of the increase in photocatalytic activity, along with the different spatial distributions of active sites imaged at the single-particle level, we propose that the ascorbic acid ligands play the following role during photocatalysis. As a sacrificial reductant, surface-adsorbed ascorbic acid molecules can be oxidized by photogenerated holes in the valence band of the $W_{18}O_{49}$ nanowires.[75,76] The remaining photogenerated electrons in the conduction band then reduce tungsten ions exposed at the surface of the nanowires. This redox process requires the creation of new oxygen vacancies to maintain charge balance, which serve as new active sites for photocatalytic •OH generation. As the ligands decompose during the reaction (based on IR and NMR spectra, see Figures S6 and S17), they no longer block access to the surface of the nanowires. This mechanism explains the significant boost of the photocatalytic activity as well as the high degree of colocalization between APF and FA activity maps. We hypothesized other electron-donating ligands could activate the $W_{18}O_{49}$ nanowires.[77,78] Indeed, we observed that citrate-functionalized $W_{18}O_{49}$ nanowires also produce the same

https://doi.org/10.1021/acs.nanolett.2c00674
Nano Lett. 2022, 22, 4694−4701

changes in single-molecule activity maps as observed for ascorbic acid (Figure S19, Figure S21, and Table S3).

In summary, using *in situ*, single-molecule fluorescence microscopy in combination with ensemble surface characterization, we developed new insights into the role of surface-adsorbed organic ligands during semiconductor photocatalysis. Reductive ligands, such as ascorbic acid, generate new oxygen vacancies in a metal oxide semiconductor during photocatalysis and activate the catalyst for oxidation. While sterically bulky organic ligands are often needed to maintain colloidal stability, they can also block access to the nanocrystal surface. We show that redox-active ligands can generate new active sites *in situ* on the nanocrystal surface during photocatalysis. Therefore, mixed monolayers that combine inert, long-chain surfactants with redox-active ligands that boost activity may provide a strategy to both maintain colloidal stability during photocatalysis and create a high number of actives sites.

■ ASSOCIATED CONTENT

Supporting Information

The Supporting Information is available free of charge at https://pubs.acs.org/doi/10.1021/acs.nanolett.2c00674.

Additional experimental details on the materials used in these experiments, structural characterization of the $W_{18}O_{49}$ nanowires, sample preparation and instrumentation for single-molecule fluorescence microscopy, analysis and processing of super-resolution images, and colocalization analysis; additional discussion of the binding of ascorbic acid to the nanowires and its degradation during photocatalysis; additional figures providing characterization of $W_{18}O_{49}$ nanowires by XRD, high-resolution TEM, XPS, absorption spectroscopy, and FT-IR spectroscopy; ensemble fluorescence spectra for the activation of APF and coumarin; ensemble photocatalytic activities for water oxidation using different samples of $W_{18}O_{49}$ nanowires; quantitative characterization of APF and furfuryl alcohol fluorescence bursts on $W_{18}O_{49}$ nanowires during single-molecule imaging; super-resolution activity maps and colocalization analysis of additional nanowires; reaction scheme for the activation of furfuryl alcohol; NMR spectroscopy of irradiated solutions containing $W_{18}O_{49}$ nanowires and ascorbic acid; single-molecule imaging and concentration dependence showing the recovery in photocatalytic activity for oxidized nanowires after functionalization; concentration dependence of the on-times for fluorescence bursts using APF; concentration dependence of specific activity for functionalized nanowires; distribution of the specific activity for different bins before and after functionalization; tables providing the conditions used for ensemble fluorescence spectroscopy, the surface properties of different nanowire samples, and reaction constants obtained from single-molecule imaging (PDF)

■ AUTHOR INFORMATION

Corresponding Author

Bryce Sadtler − *Department of Chemistry, Washington University, St. Louis, Missouri 63130, United States; Institute of Materials Science and Engineering, Washington University, St. Louis, Missouri 63130, United States;* orcid.org/0000-0003-4860-501X; Email: sadtler@wustl.edu

Authors

Meikun Shen − *Department of Chemistry, Washington University, St. Louis, Missouri 63130, United States;* orcid.org/0000-0001-8100-4115

Tianben Ding − *Department of Electrical and Systems Engineering, Washington University, St. Louis, Missouri 63130, United States;* orcid.org/0000-0003-0710-2344

Che Tan − *Department of Energy, Environmental, and Chemical Engineering, Washington University, St. Louis, Missouri 63130, United States*

William H. Rackers − *Department of Chemistry, Washington University, St. Louis, Missouri 63130, United States;* orcid.org/0000-0002-1658-2389

Dongyan Zhang − *Department of Chemistry, Washington University, St. Louis, Missouri 63130, United States;* orcid.org/0000-0002-6072-9149

Matthew D. Lew − *Department of Electrical and Systems Engineering and Institute of Materials Science and Engineering, Washington University, St. Louis, Missouri 63130, United States;* orcid.org/0000-0002-5614-3292

Complete contact information is available at: https://pubs.acs.org/10.1021/acs.nanolett.2c00674

Notes

The authors declare no competing financial interest.

■ ACKNOWLEDGMENTS

This material is based upon work supported by the National Science Foundation (NSF) under Grant CHE-1753344 to B.S. and under Grant ECCS-1653777 to M.D.L. X-ray photoelectron spectroscopy and high-resolution transmission electron microscopy were performed at the Institute of Materials Science and Engineering at Washington University. Transmission electron microscopy and zeta potential measurements were performed at the Nano Research and Environmental Facility at Washington University. X-ray diffraction was performed in the Department of Earth and Planetary Sciences at Washington University. The authors thank Z. Wang for performing the zeta potential experiments and H. Li for assistance with transmission electron microscopy.

■ REFERENCES

(1) Gordon, T. R.; Cargnello, M.; Paik, T.; Mangolini, F.; Weber, R. T.; Fornasiero, P.; Murray, C. B. Nonaqueous Synthesis of TiO_2 Nanocrystals Using TiF_4 to Engineer Morphology, Oxygen Vacancy Concentration, and Photocatalytic Activity. *J. Am. Chem. Soc.* **2012**, *134*, 6751−6761.

(2) Lu, H.; Zhu, X.; Miller, C.; San Martin, J.; Chen, X.; Miller, E. M.; Yan, Y.; Beard, M. C. Enhanced Photoredox Activity of $CsPbBr_3$ Nanocrystals by Quantitative Colloidal Ligand Exchange. *J. Chem. Phys.* **2019**, *151*, 204305.

(3) Jana, A.; Lawrence, K. N.; Teunis, M. B.; Mandal, M.; Kumbhar, A.; Sardar, R. Investigating the Control by Quantum Confinement and Surface Ligand Coating of Photocatalytic Efficiency in Chalcopyrite Copper Indium Diselenide Nanocrystals. *Chem. Mater.* **2016**, *28*, 1107−1120.

(4) Vela, J. Molecular Chemistry to the Fore: New Insights into the Fascinating World of Photoactive Colloidal Semiconductor Nanocrystals. *J. Phys. Chem. Lett.* **2013**, *4*, 653−668.

(5) Weiss, E. A. Designing the Surfaces of Semiconductor Quantum Dots for Colloidal Photocatalysis. *ACS Energy Letters* **2017**, *2*, 1005−1013.

(6) Wilker, M. B.; Utterback, J. K.; Greene, S.; Brown, K. A.; Mulder, D. W.; King, P. W.; Dukovic, G. Role of Surface-Capping Ligands in

Photoexcited Electron Transfer between CdS Nanorods and [FeFe] Hydrogenase and the Subsequent H_2 Generation. *J. Phys. Chem. C* **2018**, *122*, 741−750.
(7) Zhu, W.; Shen, M.; Fan, G.; Yang, A.; Meyer, J. R.; Ou, Y.; Yin, B.; Fortner, J.; Foston, M.; Li, Z.; Zou, Z.; Sadtler, B. Facet-Dependent Enhancement in the Activity of Bismuth Vanadate Microcrystals for the Photocatalytic Conversion of Methane to Methanol. *ACS Applied Nano Materials* **2018**, *1*, 6683−6691.
(8) Jiang, Y.; Wang, C.; Rogers, C. R.; Kodaimati, M. S.; Weiss, E. A. Regio- and Diastereoselective Intermolecular [2 + 2] Cycloadditions Photocatalysed by Quantum Dots. *Nat. Chem.* **2019**, *11*, 1034−1040.
(9) Burke, R.; Bren, K. L.; Krauss, T. D. Semiconductor Nanocrystal Photocatalysis for the Production of Solar Fuels. *J. Chem. Phys.* **2021**, *154*, 030901.
(10) McDonald, K. D.; Bartlett, B. M. Photocatalytic Primary Alcohol Oxidation on WO_3 Nanoplatelets. *RSC Adv.* **2019**, *9*, 28688−28694.
(11) Takata, T.; Jiang, J.; Sakata, Y.; Nakabayashi, M.; Shibata, N.; Nandal, V.; Seki, K.; Hisatomi, T.; Domen, K. Photocatalytic Water Splitting with a Quantum Efficiency of Almost Unity. *Nature* **2020**, *581*, 411−414.
(12) Wei, L.; Adamson, M. A. S.; Vela, J. Ni_2P-Modified Ta_3N_5 and TaON for Photocatalytic Nitrate Reduction. *ChemNanoMat* **2020**, *6*, 1179−1185.
(13) Burke, R.; Chakraborty, S.; McClelland, K. P.; Jelušić, J.; Matson, E. M.; Bren, K. L.; Krauss, T. D. Light-Driven Hydrogen Production with CdSe Quantum Dots and a Cobalt Glutathione Catalyst. *Chem. Commun.* **2021**, *57*, 2053−2056.
(14) Xi, G.; Ouyang, S.; Li, P.; Ye, J.; Ma, Q.; Su, N.; Bai, H.; Wang, C. Ultrathin $W_{18}O_{49}$ Nanowires with Diameters Below 1 nm: Synthesis, Near-Infrared Absorption, Photoluminescence, and Photochemical Reduction of Carbon Dioxide. *Angew. Chem., Int. Ed.* **2012**, *51*, 2395−2399.
(15) Yan, J.; Wang, T.; Wu, G.; Dai, W.; Guan, N.; Li, L.; Gong, J. Tungsten Oxide Single Crystal Nanosheets for Enhanced Multichannel Solar Light Harvesting. *Adv. Mater.* **2015**, *27*, 1580−1586.
(16) Huang, Z.-F.; Song, J.; Pan, L.; Zhang, X.; Wang, L.; Zou, J.-J. Tungsten Oxides for Photocatalysis, Electrochemistry, and Phototherapy. *Adv. Mater.* **2015**, *27*, 5309−5327.
(17) Zhang, N.; Li, X.; Ye, H.; Chen, S.; Ju, H.; Liu, D.; Lin, Y.; Ye, W.; Wang, C.; Xu, Q.; Zhu, J.; Song, L.; Jiang, J.; Xiong, Y. Oxide Defect Engineering Enables to Couple Solar Energy into Oxygen Activation. *J. Am. Chem. Soc.* **2016**, *138*, 8928−8935.
(18) Kim, J.; Lee, C. W.; Choi, W. Platinized WO_3 as an Environmental Photocatalyst That Generates OH Radicals under Visible Light. *Environ. Sci. Technol.* **2010**, *44*, 6849−6854.
(19) Liang, L.; Li, X.; Sun, Y.; Tan, Y.; Jiao, X.; Ju, H.; Qi, Z.; Zhu, J.; Xie, Y. Infrared Light-Driven CO_2 Overall Splitting at Room Temperature. *Joule* **2018**, *2*, 1004−1016.
(20) Zhang, N.; Jalil, A.; Wu, D.; Chen, S.; Liu, Y.; Gao, C.; Ye, W.; Qi, Z.; Ju, H.; Wang, C.; Wu, X.; Song, L.; Zhu, J.; Xiong, Y. Refining Defect States in $W_{18}O_{49}$ by Mo Doping: A Strategy for Tuning N_2 Activation Towards Solar-Driven Nitrogen Fixation. *J. Am. Chem. Soc.* **2018**, *140*, 9434−9443.
(21) Klahr, B. M.; Hamann, T. W. Current and Voltage Limiting Processes in Thin Film Hematite Electrodes. *J. Phys. Chem. C* **2011**, *115*, 8393−8399.
(22) Pala, R. A.; Leenheer, A. J.; Lichterman, M.; Atwater, H. A.; Lewis, N. S. Measurement of Minority-Carrier Diffusion Lengths Using Wedge-Shaped Semiconductor Photoelectrodes. *Energy Environ. Sci.* **2014**, *7*, 3424−3430.
(23) Irgen-Gioro, S.; Yang, M.; Padgaonkar, S.; Chang, W. J.; Zhang, Z.; Nagasing, B.; Jiang, Y.; Weiss, E. A. Charge and Energy Transfer in the Context of Colloidal Nanocrystals. *Chemical Physics Reviews* **2020**, *1*, 011305.
(24) Yin, Y.; Alivisatos, A. P. Colloidal Nanocrystal Synthesis and the Organic−Inorganic Interface. *Nature* **2005**, *437*, 664−670.
(25) Owen, J. The Coordination Chemistry of Nanocrystal Surfaces. *Science* **2015**, *347*, 615−616.
(26) Boles, M. A.; Ling, D.; Hyeon, T.; Talapin, D. V. The Surface Science of Nanocrystals. *Nat. Mater.* **2016**, *15*, 141−153.
(27) Heuer-Jungemann, A.; Feliu, N.; Bakaimi, I.; Hamaly, M.; Alkilany, A.; Chakraborty, I.; Masood, A.; Casula, M. F.; Kostopoulou, A.; Oh, E.; Susumu, K.; Stewart, M. H.; Medintz, I. L.; Stratakis, E.; Parak, W. J.; Kanaras, A. G. The Role of Ligands in the Chemical Synthesis and Applications of Inorganic Nanoparticles. *Chem. Rev.* **2019**, *119*, 4819−4880.
(28) Rossi, L. M.; Fiorio, J. L.; Garcia, M. A. S.; Ferraz, C. P. The Role and Fate of Capping Ligands in Colloidally Prepared Metal Nanoparticle Catalysts. *Dalton Transactions* **2018**, *47*, 5889−5915.
(29) Marshall, S. T.; O'Brien, M.; Oetter, B.; Corpuz, A.; Richards, R. M.; Schwartz, D. K.; Medlin, J. W. Controlled Selectivity for Palladium Catalysts Using Self-Assembled Monolayers. *Nat. Mater.* **2010**, *9*, 853−858.
(30) Kahsar, K. R.; Schwartz, D. K.; Medlin, J. W. Selective Hydrogenation of Polyunsaturated Fatty Acids Using Alkanethiol Self-Assembled Monolayer-Coated Pd/Al_2O_3 Catalysts. *ACS Catal.* **2013**, *3*, 2041−2044.
(31) Jones, S.; Qu, J.; Tedsree, K.; Gong, X.-Q.; Tsang, S. C. E. Prominent Electronic and Geometric Modifications of Palladium Nanoparticles by Polymer Stabilizers for Hydrogen Production under Ambient Conditions. *Angew. Chem., Int. Ed.* **2012**, *51*, 11275−11278.
(32) Tong, Y. J. Unconventional Promoters of Catalytic Activity in Electrocatalysis. *Chem. Soc. Rev.* **2012**, *41*, 8195−8209.
(33) Zhou, Z.-Y.; Kang, X.; Song, Y.; Chen, S. Ligand-Mediated Electrocatalytic Activity of Pt Nanoparticles for Oxygen Reduction Reactions. *J. Phys. Chem. C* **2012**, *116*, 10592−10598.
(34) Chung, Y.-H.; Chung, D. Y.; Jung, N.; Sung, Y.-E. Tailoring the Electronic Structure of Nanoelectrocatalysts Induced by a Surface-Capping Organic Molecule for the Oxygen Reduction Reaction. *J. Phys. Chem. Lett.* **2013**, *4*, 1304−1309.
(35) Chung, Y.-H.; Kim, S. J.; Chung, D. Y.; Park, H. Y.; Sung, Y.-E.; Yoo, S. J.; Jang, J. H. Third-Body Effects of Native Surfactants on Pt Nanoparticle Electrocatalysts in Proton Exchange Fuel Cells. *Chem. Commun.* **2015**, *51*, 2968−2971.
(36) Wan, X.-K.; Wang, J.-Q.; Nan, Z.-A.; Wang, Q.-M. Ligand Effects in Catalysis by Atomically Precise Gold Nanoclusters. *Science Advances* **2017**, *3*, No. e1701823.
(37) Fiorio, J. L.; López, N.; Rossi, L. M. Gold−Ligand-Catalyzed Selective Hydrogenation of Alkynes into Cis-Alkenes Via H_2 Heterolytic Activation by Frustrated Lewis Pairs. *ACS Catal.* **2017**, *7*, 2973−2980.
(38) Benson, E. E.; Zhang, H.; Schuman, S. A.; Nanayakkara, S. U.; Bronstein, N. D.; Ferrere, S.; Blackburn, J. L.; Miller, E. M. Balancing the Hydrogen Evolution Reaction, Surface Energetics, and Stability of Metallic MoS_2 Nanosheets Via Covalent Functionalization. *J. Am. Chem. Soc.* **2018**, *140*, 441−450.
(39) De Roo, J.; Huang, Z.; Schuster, N. J.; Hamachi, L. S.; Congreve, D. N.; Xu, Z.; Xia, P.; Fishman, D. A.; Lian, T.; Owen, J. S.; Tang, M. L. Anthracene Diphosphate Ligands for CdSe Quantum Dots; Molecular Design for Efficient Upconversion. *Chem. Mater.* **2020**, *32*, 1461−1466.
(40) Ung, D.; Cossairt, B. M. Effect of Surface Ligands on CoP for the Hydrogen Evolution Reaction. *ACS Applied Energy Materials* **2019**, *2*, 1642−1645.
(41) Westmoreland, D. E.; López-Arteaga, R.; Weiss, E. A. N-Heterocyclic Carbenes as Reversible Exciton-Delocalizing Ligands for Photoluminescent Quantum Dots. *J. Am. Chem. Soc.* **2020**, *142*, 2690−2696.
(42) Pankhurst, J. R.; Iyengar, P.; Loiudice, A.; Mensi, M.; Buonsanti, R. Metal−Ligand Bond Strength Determines the Fate of Organic Ligands on the Catalyst Surface During the Electrochemical CO_2 Reduction Reaction. *Chemical Science* **2020**, *11*, 9296−9302.
(43) Roeffaers, M. B. J.; De Cremer, G.; Libeert, J.; Ameloot, R.; Dedecker, P.; Bons, A.-J.; Bückins, M.; Martens, J. A.; Sels, B. F.; De Vos, D. E.; Hofkens, J. Super-Resolution Reactivity Mapping of Nanostructured Catalyst Particles. *Angew. Chem., Int. Ed.* **2009**, *48*, 9285−9289.

https://doi.org/10.1021/acs.nanolett.2c00674
Nano Lett. 2022, 22, 4694−4701

(44) Ristanović, Z.; Hofmann, J. P.; De Cremer, G.; Kubarev, A. V.; Rohnke, M.; Meirer, F.; Hofkens, J.; Roeffaers, M. B. J.; Weckhuysen, B. M. Quantitative 3D Fluorescence Imaging of Single Catalytic Turnovers Reveals Spatiotemporal Gradients in Reactivity of Zeolite H-ZSM-5 Crystals Upon Steaming. *J. Am. Chem. Soc.* **2015**, *137*, 6559−6568.
(45) Hendriks, F. C.; Mohammadian, S.; Ristanović, Z.; Kalirai, S.; Meirer, F.; Vogt, E. T. C.; Bruijnincx, P. C. A.; Gerritsen, H. C.; Weckhuysen, B. M. Integrated Transmission Electron and Single-Molecule Fluorescence Microscopy Correlates Reactivity with Ultrastructure in a Single Catalyst Particle. *Angew. Chem., Int. Ed.* **2018**, *57*, 257−261.
(46) Wang, N.; Tachikawa, T.; Majima, T. Single-Molecule, Single-Particle Observation of Size-Dependent Photocatalytic Activity in Au/TiO_2 Nanocomposites. *Chemical Science* **2011**, *2*, 891−900.
(47) Tachikawa, T.; Yamashita, S.; Majima, T. Evidence for Crystal-Face-Dependent TiO_2 Photocatalysis from Single-Molecule Imaging and Kinetic Analysis. *J. Am. Chem. Soc.* **2011**, *133*, 7197−7204.
(48) Wang, W.-K.; Chen, J.-J.; Lou, Z.-Z.; Kim, S.; Fujitsuka, M.; Yu, H.-Q.; Majima, T. Single-Molecule and -Particle Probing Crystal Edge/Corner as Highly Efficient Photocatalytic Sites on a Single TiO_2 Particle. *Proc. Natl. Acad. Sci. U. S. A.* **2019**, *116*, 18827−18833.
(49) Xu, W.; Jain, P. K.; Beberwyck, B. J.; Alivisatos, A. P. Probing Redox Photocatalysis of Trapped Electrons and Holes on Single Sb-Doped Titania Nanorod Surfaces. *J. Am. Chem. Soc.* **2012**, *134*, 3946−3949.
(50) Sambur, J. B.; Chen, T.-Y.; Choudhary, E.; Chen, G.; Nissen, E. J.; Thomas, E. M.; Zou, N.; Chen, P. Sub-Particle Reaction and Photocurrent Mapping to Optimize Catalyst-Modified Photoanodes. *Nature* **2016**, *530*, 77−80.
(51) Mao, X.; Liu, C.; Hesari, M.; Zou, N.; Chen, P. Super-Resolution Imaging of Non-Fluorescent Reactions Via Competition. *Nat. Chem.* **2019**, *11*, 687−694.
(52) Ye, R.; Zhao, M.; Mao, X.; Wang, Z.; Garzón, D. A.; Pu, H.; Zhao, Z.; Chen, P. Nanoscale Cooperative Adsorption for Materials Control. *Nat. Commun.* **2021**, *12*, 4287.
(53) Ha, J. W.; Ruberu, T. P. A.; Han, R.; Dong, B.; Vela, J.; Fang, N. Super-Resolution Mapping of Photogenerated Electron and Hole Separation in Single Metal−Semiconductor Nanocatalysts. *J. Am. Chem. Soc.* **2014**, *136*, 1398−1408.
(54) Xu, W.; Kong, J. S.; Yeh, Y.-T. E.; Chen, P. Single-Molecule Nanocatalysis Reveals Heterogeneous Reaction Pathways and Catalytic Dynamics. *Nat. Mater.* **2008**, *7*, 992−996.
(55) Andoy, N. M.; Zhou, X.; Choudhary, E.; Shen, H.; Liu, G.; Chen, P. Single-Molecule Catalysis Mapping Quantifies Site-Specific Activity and Uncovers Radial Activity Gradient on Single 2D Nanocrystals. *J. Am. Chem. Soc.* **2013**, *135*, 1845−1852.
(56) Chen, T.; Zhang, Y.; Xu, W. Single-Molecule Nanocatalysis Reveals Catalytic Activation Energy of Single Nanocatalysts. *J. Am. Chem. Soc.* **2016**, *138*, 12414−12421.
(57) Chen, T.; Dong, B.; Chen, K.; Zhao, F.; Cheng, X.; Ma, C.; Lee, S.; Zhang, P.; Kang, S. H.; Ha, J. W.; Xu, W.; Fang, N. Optical Super-Resolution Imaging of Surface Reactions. *Chem. Rev.* **2017**, *117*, 7510−7537.
(58) Wilson, A. J.; Willets, K. A. Visualizing Site-Specific Redox Potentials on the Surface of Plasmonic Nanoparticle Aggregates with Superlocalization SERS Microscopy. *Nano Lett.* **2014**, *14*, 939−945.
(59) An, J.; Song, X.; Wan, W.; Chen, Y.; Si, H.; Duan, H.; Li, L.; Tang, B. Kinetics of the Photoelectron-Transfer Process Characterized by Real-Time Single-Molecule Fluorescence Imaging on Individual Photocatalyst Particles. *ACS Catal.* **2021**, *11*, 6872−6882.
(60) Liu, Y.; Zhang, K.; Tian, X.; Zhou, L.; Liu, J.; Liu, B. Quantitative Single-Particle Fluorescence Imaging Elucidates Semiconductor Shell Influence on Ag@TiO_2 Photocatalysis. *ACS Appl. Mater. Interfaces* **2021**, *13*, 7680−7687.
(61) Shen, M.; Ding, T.; Rackers, W. H.; Tan, C.; Mahmood, K.; Lew, M. D.; Sadtler, B. Single-Molecule Colocalization of Redox Reactions on Semiconductor Photocatalysts Connects Surface Heterogeneity and Charge-Carrier Separation in Bismuth Oxybromide. *J. Am. Chem. Soc.* **2021**, *143*, 11393−11403.
(62) Shen, M.; Ding, T.; Hartman, S. T.; Wang, F.; Krucylak, C.; Wang, Z.; Tan, C.; Yin, B.; Mishra, R.; Lew, M. D.; Sadtler, B. Nanoscale Colocalization of Fluorogenic Probes Reveals the Role of Oxygen Vacancies in the Photocatalytic Activity of Tungsten Oxide Nanowires. *ACS Catal.* **2020**, *10*, 2088−2099.
(63) Shen, M.; Ding, T.; Luo, J.; Tan, C.; Mahmood, K.; Wang, Z.; Zhang, D.; Mishra, R.; Lew, M. D.; Sadtler, B. Competing Activation and Deactivation Mechanisms in Photodoped Bismuth Oxybromide Nanoplates Probed by Single-Molecule Fluorescence Imaging. *J. Phys. Chem. Lett.* **2020**, *11*, 5219−5227.
(64) Dong, B.; Pei, Y.; Zhao, F.; Goh, T. W.; Qi, Z.; Xiao, C.; Chen, K.; Huang, W.; Fang, N. In Situ Quantitative Single-Molecule Study of Dynamic Catalytic Processes in Nanoconfinement. *Nature Catalysis* **2018**, *1*, 135−140.
(65) Garcia, A., IV; Saluga, S. J.; Dibble, D. J.; López, P. A.; Saito, N.; Blum, S. A. Does Selectivity of Molecular Catalysts Change with Time? Polymerization Imaged by Single-Molecule Spectroscopy. *Angew. Chem., Int. Ed.* **2021**, *60*, 1550−1555.
(66) Eivgi, O.; Blum, S. A. Exploring Chemistry with Single-Molecule and -Particle Fluorescence Microscopy. *Trends in Chemistry* **2022**, *4*, 5−14.
(67) Wenderich, K.; Noack, J.; Kärgel, A.; Trunschke, A.; Mul, G. Effect of Temperature and pH on Phase Transformations in Citric Acid Mediated Hydrothermal Growth of Tungsten Oxide. *Eur. J. Inorg. Chem.* **2018**, *2018*, 917−923.
(68) Dahl, J. A.; Maddux, B. L. S.; Hutchison, J. E. Toward Greener Nanosynthesis. *Chem. Rev.* **2007**, *107*, 2228−2269.
(69) Guo, C.; Yin, S.; Yan, M.; Kobayashi, M.; Kakihana, M.; Sato, T. Morphology-Controlled Synthesis of $W_{18}O_{49}$ Nanostructures and Their Near-Infrared Absorption Properties. *Inorg. Chem.* **2012**, *51*, 4763−4771.
(70) Zhang, J.; Nosaka, Y. Mechanism of the OH Radical Generation in Photocatalysis with TiO_2 of Different Crystalline Types. *J. Phys. Chem. C* **2014**, *118*, 10824−10832.
(71) Hu, J.; Zhao, X.; Chen, W.; Su, H.; Chen, Z. Theoretical Insight into the Mechanism of Photoelectrochemical Oxygen Evolution Reaction on $BiVO_4$ Anode with Oxygen Vacancy. *J. Phys. Chem. C* **2017**, *121*, 18702−18709.
(72) Gomes, A.; Fernandes, E.; Lima, J. L. F. C. Fluorescence Probes Used for Detection of Reactive Oxygen Species. *Journal of Biochemical and Biophysical Methods* **2005**, *65*, 45−80.
(73) Xu, Y.; Schoonen, M. A. A. The Absolute Energy Positions of Conduction and Valence Bands of Selected Semiconducting Minerals. *Am. Mineral.* **2000**, *85*, 543−556.
(74) Malkusch, S.; Endesfelder, U.; Mondry, J.; Gelléri, M.; Verveer, P. J.; Heilemann, M. Coordinate-Based Colocalization Analysis of Single-Molecule Localization Microscopy Data. *Histochemistry and Cell Biology* **2012**, *137*, 1−10.
(75) Zeng, Y.; Kelley, D. F. Excited Hole Photochemistry of CdSe/CdS Quantum Dots. *J. Phys. Chem. C* **2016**, *120*, 17853−17862.
(76) Shulenberger, K. E.; Keller, H. R.; Pellows, L. M.; Brown, N. L.; Dukovic, G. Photocharging of Colloidal CdS Nanocrystals. *J. Phys. Chem. C* **2021**, *125*, 22650−22659.
(77) Xue, C.; Métraux, G. S.; Millstone, J. E.; Mirkin, C. A. Mechanistic Study of Photomediated Triangular Silver Nanoprism Growth. *J. Am. Chem. Soc.* **2008**, *130*, 8337−8344.
(78) Thrall, E. S.; Preska Steinberg, A.; Wu, X.; Brus, L. E. The Role of Photon Energy and Semiconductor Substrate in the Plasmon-Mediated Photooxidation of Citrate by Silver Nanoparticles. *J. Phys. Chem. C* **2013**, *117*, 26238−26247.

https://doi.org/10.1021/acs.nanolett.2c00674
Nano Lett. 2022, 22, 4694−4701